Thermal Conductivity of Methane Hydrate from Experiment and Molecular Simulation

Eilis J. Rosenbaum,[†,‡] Niall J. English,*[,†,§,||] J. Karl Johnson,[†,§] David W. Shaw,[†,⊥] and Robert P. Warzinski*[,†]

National Energy Technology Laboratory, United States Department of Energy, P.O. Box 10940, Pittsburgh, Pennsylvania 15236, NETL Support Contractor, Parsons, P.O. Box 618, South Park, Pennsylvania 15129, Department of Chemical and Petroleum Engineering, University of Pittsburgh, Pittsburgh, Pennsylvania 15261, and Geneva College, Department of Engineering, 3200 College Avenue, Beaver Falls, Pennsylvania 15010

Received: June 7, 2007; In Final Form: August 13, 2007

A single-sided transient plane source technique has been used to determine the thermal conductivity and thermal diffusivity of a compacted methane hydrate sample over the temperature range of 261.5−277.4 K and at gas-phase pressures ranging from 3.8 to 14.2 MPa. The average thermal conductivity, 0.68 ± 0.01 W/(m·K), and thermal diffusivity, $2.04 \times 10^{-7} \pm 0.04 \times 10^{-7}$ m^2/s, values are, respectively, higher and lower than previously reported values. Equilibrium molecular dynamics (MD) simulations of methane hydrate have also been performed in the NPT ensemble to estimate the thermal conductivity for methane compositions ranging from 80 to 100% of the maximum theoretical occupation, at 276 K and at pressures ranging from 0.1 to 100 MPa. Calculations were performed with three rigid potential models for water, namely, SPC/E, TIP4P-Ew, and TIP4P-FQ, the last of which includes the effects of polarizability. The thermal conductivities predicted from MD simulations were in reasonable agreement with experimental results, ranging from about 0.52 to 0.77 W/(m·K) for the different potential models with the polarizable water model giving the best agreement with experiments. The MD simulation method was validated by comparing calculated and experimental thermal conductivity values for ice and liquid water. The simulations were in reasonable agreement with experimental data. The simulations predict a slight increase in the thermal conductivity with decreasing methane occupation of the hydrate cages. The thermal conductivity was found to be essentially independent of pressure in both simulations and experiments. Our experimental and simulation thermal conductivity results provide data to help predict gas hydrate stability in sediments for the purposes of production or estimating methane release into the environment due to gradual warming.

Introduction

The fairly recent discovery of enormous quantities of natural gas as gas hydrates in sub-oceanic sediments and permafrost formations has stimulated significant interest in their use as a resource, as a potential geohazard, in their role in the global carbon cycle, and as a potential climate influence.[1−3] Progress in research in these areas is fundamentally dependent on the availability of high-quality property data and on an increased understanding of the physics and chemistry that govern gas hydrates in nature.[4] One key knowledge gap is in thermal property data, with the number of these measurements being several orders of magnitude less than that for phase equilibrium properties.[1,2] The importance of reliable thermal property data for modeling the behavior of gas hydrates in natural systems has been discussed by Sloan,[1] Gupta et al.,[5] and Waite et al.[2]

Measuring the thermal properties of relatively pure methane hydrate at the temperatures of interest for production and climate change scenarios requires the use of pressurized equipment to both form the samples in the laboratory and stabilize them during measurement. It is also desirable to reduce the porosity of the sample after formation by compaction in the same pressure vessel. Removal of the sample for compaction introduces the possibility of contamination or decomposition of the hydrate during transfer and handling.

Most of the measurements of thermal conductivity reported for methane hydrate in the literature have been made using a needle probe on samples prepared using granular ice.[2,6,7] However, recent work has been reported using a commercially available transient plane source (TPS) technique[8] in a double-sided configuration as developed by Gustaffson.[9,10] The measured values of thermal conductivity for compacted samples of methane hydrate at conditions similar to those in natural environments have ranged from 0.46 W/(m·K) (ref 7) to 0.62 W/(m·K) (ref 2) using a needle probe to 0.57 W/(m·K) using the double-sided TPS technique in which hydrate was formed from methane and water that contained a surfactant to assist hydrate formation.[8] Measures of the thermal diffusivity of methane hydrate have been reported by Kumar et al.[11] and Turner et al.[12] for porous samples (uncompacted) and by deMartin[6] and Waite et al.[2] for compacted samples. The thermal diffusivity values do not seem to be dependent on the presence of some porosities and are close to 3.1×10^{-7} m^2/s.[2] All of these measurement techniques require the needle probe or TPS to be surrounded by the hydrate. While practical in the laboratory, such technology may not be easily adapted for in-

* Corresponding authors. E-mail: (N.J.E.) niall.english@ucd.ie and (R.P.W.) robert.warzinski@netl.doe.gov.
[†] National Energy Technology Laboratory.
[‡] Parsons.
[§] University of Pittsburgh.
[||] Current address: School of Chemical and Bioprocess Engineering, The Centre for Synthesis and Chemical Biology, Conway Institute of Biomolecular and Biomedical Research, University College Dublin, Belfield, Dublin 4, Ireland.
[⊥] Geneva College.

10.1021/jp074419o CCC: $37.00
Published on Web 10/30/2007

situ determination of the thermal properties of methane hydrate or consolidated methane hydrate/sediment samples. The motivation behind the experimental work in this paper is to develop a device that can make a contact measurement without requiring penetration of a sample and that could be adapted for field use. A single-sided TPS technique is reported in this work.

Gas hydrates, in general, exhibit an anomalous, glass-like behavior of thermal conductivity that distinguishes them from ice and other molecular crystals.[13] A detailed understanding of the mechanisms leading to this behavior would enhance the underlying knowledge of hydrate physics that may lead to improvements in simulation programs for determining long-term resource recovery potential and the impact of hydrate on climate change. It is thought that the low thermal conductivity is attributable to the phonon-scattering processes from energy transfer between the localized guest rattling modes and the host lattice acoustic modes.[14−18] A detailed understanding of the mechanisms leading to this behavior, in addition to characterization of hydrate thermophysical properties,[4] would enhance the viability of large-scale methane production from hydrates.[19,20]

The goals of the equilibrium molecular dynamics (MD) studies reported here are 4-fold: (1) assess the ability of a variety of water potential models to estimate the thermal conductivity of methane hydrate with respect to experimental measurements; (2) gauge the influence of explicit polarizability on calculated thermal conductivities; (3) measure the influence of methane occupation on the thermal conductivity; and (4) test the effect of external (isotropic) pressure on thermal conductivity. Calculations were carried out for different methane compositions at 276 K and at a variety of pressures from 0.1 to 100 MPa. The MD simulation method was validated by the estimation of thermal conductivity for ice and liquid water and comparison with experimental data.

Experimental Procedures

The thermal conductivity of a laboratory prepared methane hydrate sample was measured using a single-sided TPS technique in a high-pressure thermal property measurement device (HTMD), that was developed at the National Energy Technology Laboratory (NETL). This device permits the formation and subsequent direct compaction of the sample on a TPS element attached to an insulating support. The sample was formed from 99.999% methane and 18 MΩ-cm water purified by reverse osmosis and ion exchange in a specially designed cup, which also permitted compaction of the sample at a constant gas pressure via an internal hydraulically actuated piston. The presence of nearly pure methane hydrate in similar samples formed in the HTMD has been confirmed by Raman spectroscopy.[21]

A schematic of the HTMD is shown in Figure 1. Figure 1A depicts the cup assembly as it is situated in a pressure vessel that contains an internal piston that is used to change the internal volume of the device and to press on the top of the cup assembly to directly compact the sample inside it.

More details of the cup assembly are shown in Figure 1B. It consists of four separable components. A base is used to affix the assembly to a stainless steel disk that is part of the pressure vessel (Figure 1A). A cup bottom is indexed to the base to permit alignment of gold-plated contacts in the base and bottom. The cup bottom also contains the TPS element, which is adhered to its top surface with Instabond S-100 cyanoacrylate adhesive. A diagram of the TPS used is shown in Figure 2. It is an ETG-50B nickel temperature sensor with a flexible polyimide encapsulation carrier obtained from Vishay Micro-Measure-

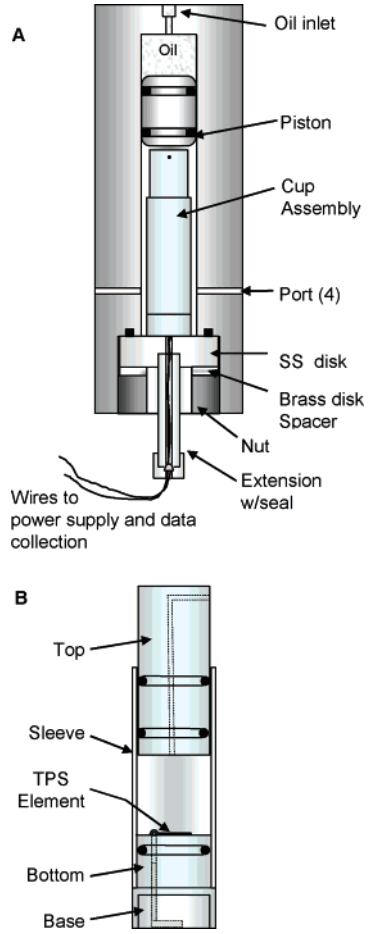

Figure 1. HTMD with cup assembly (A) and schematic of cup assembly (B).

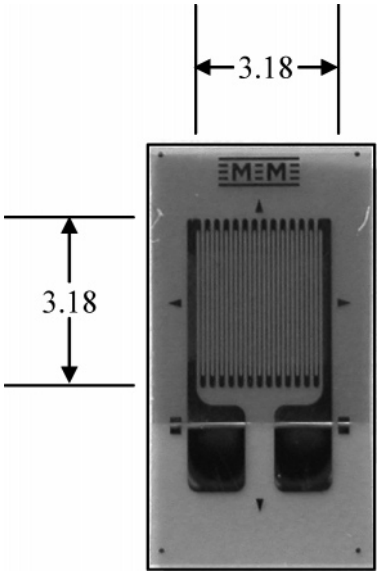

Figure 2. TPS element (dimensions are in millimeters).

ments, Inc. 34-AWG wires were soldered to both exposed solder tabs on the sensor and the female gold contacts in the bottom. The solder joints to the TPS element were protectively coated, typically with Gagekote #1 and M Coat B, also from Vishay Micro-Measurements, Inc. A sleeve was fitted over the bottom and rested on the base. A cup top was fitted inside the sleeve. Nitrile o-rings were used to seal the bottom and top inside the sleeve. A small hole was provided in the top to allow gas communication with the inside of the pressure vessel. It was

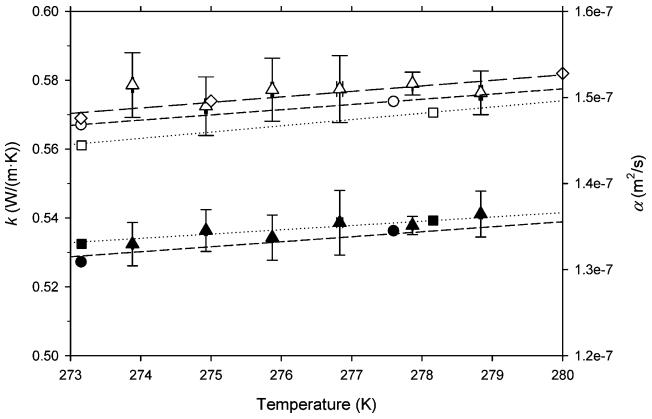

Figure 3. Comparison of thermal conductivity (filled symbols) and thermal diffusivity (solid symbols) results for water obtained with the TPS to those obtained from the literature. △, ▲: NETL data ◇: Brodkey and Hershey;[22] □, ■: NIST data;[23] ○, ●: U.S. Coast Guard.[24] Linear regressions are shown for the literature data.

drilled at a 90° angle to prevent water from escaping during hydrate decomposition. This arrangement also permitted the internal piston of the pressure vessel to press against the cup top to push it down against the sample in the cup assembly.

A platinum resistance temperature detector positioned just inside the HTMD near the cup bottom was used to monitor the temperature. A digital Heise gauge (±17 kPa accuracy) was used for pressure measurement. National Instruments Labview software was used for process control, data acquisition, and analysis.

Calibration of the TPS in the cup assembly was performed with 18 MΩ-cm water. The thermal conductivity and thermal diffusivity results are shown in Figure 3 along with reference data.[22−24] The agreement between the TPS results and the literature values illustrates the accuracy of the technique.

The experimental procedure involved adding 0.9904 g of water to the cup assembly. This was sufficient to cover the TPS element to a depth of 5.02 mm, which is greater than the probing depth calculated according to Gustafsson's equation for probing depth.[9] The cup assembly containing the water was plugged into the base and inserted into the HTMD. The HTMD was then placed into an environmental chamber that controlled the temperature of the experiment to within 0.1 K. The temperature of the chamber was lowered to around 261 K to form ice. After forming ice, and purging, methane was added and pressurized to about 5.6 MPa, and hydrate was formed by repeated cooling and heating of the HTMD at 1 K/h in the environmental chamber. This was repeated until no further gas uptake (pressure decrease) or ice formation (pressure increase) from unreacted water was evident from the pressure data (recorded at about 1/min).

The hydrate sample was then compacted with mechanical pressure by hydraulically pushing the internal piston of the pressure vessel onto the cup top, which moved down to contact and compact the sample. The compaction pressure was increased to near 50 MPa, then released incrementally, and then cycled in this manner a few times. Subsequently, the temperature of the sample was raised to above the ice melting point but within the region of hydrate stability, and the compaction was repeated several times. Finally, nearly all of the compaction pressure was removed, and the methane pressure in HTMD was varied for three different temperatures above and below the freezing point of water but within the hydrate stability zone.

Thermal conductivity (k) and thermal diffusivity (α) were simultaneously measured during all phases of the experiment according to a procedure developed by Gustafsson[9,10] for a hot square source arrangement of the TPS similar to that shown in Figure 2. The conducting pattern on the hot square consists of equally wide metallic strips made by depositing nickel in a serpentine pattern between two layers of a polyimide called Kapton. The average temperature rise of the hot square is given by Gustaffson[9] as

$$\overline{\Delta T(\tau)} = \frac{P_{av} H(\tau)}{4\pi^{1/2} a k} \tag{1}$$

where P_{av} is the average power supplied to the hot square during the measurement. $2a$ is the effective length of one side of the hot square and is arrived at by applying a factor to the nominal hot square half-length. The factor is determined through calibration. For convenience, dimensionless time, τ, is used to enable solutions in one variable and is defined as

$$\tau = \sqrt{\frac{t}{\theta}}, \theta = \frac{a^2}{\alpha} \tag{2}$$

where θ is the characteristic time of the measurement, unique to the sample being measured since it is a function of the sample α.

It is accepted that the function $H(\tau)$ in eq 1 can be approximated by[9]

$$H(\tau) = \int_0^\tau \left\{ erf\left(\frac{1}{\upsilon}\right) - \frac{\upsilon}{\sqrt{\pi}} \left[1 - \exp\left(-\frac{1}{\upsilon^2}\right)\right]\right\}^2 d\upsilon \tag{3}$$

where

$$erf(x) = \frac{2}{\sqrt{\pi}} \int_0^x \exp(-\upsilon^2) d\upsilon \tag{4}$$

By solving $H(\tau)$ numerically for a range of τ values, an empirical equation was determined for $H(\tau)$ that was used in the analysis. $H(\tau)$ can be used to obtain very accurate and reliable results. A more exact solution would take into account the thin insulating layers on both sides of the individual strips of the conducting pattern. A time correction, t_c, is applied when evaluating the transient measurements to account for the difference between the exact solution and $H(\tau)$.[9]

Equation 1 can be rearranged to solve for k. The slope of $\overline{\Delta T(\tau)}$ versus $H(\tau)$ is used in the rearranged equation to calculate k

$$k = \frac{P_{av}}{4\pi^{1/2} a} \frac{1}{\text{slope}} \tag{5}$$

$\overline{\Delta T(\tau)}$ is found from the resistance rise of the TPS during the transient measurement. The rise in the voltage difference across a Wheatstone bridge is recorded with time to find the resistance of the TPS as a function of time. The time dependent resistance of the TPS is expressed as[9]

$$R(t) = R^*[1 + (\text{TCR})\overline{\Delta T(\tau)}] \tag{6}$$

Equation 6 can be solved for $\overline{\Delta T(\tau)}$ and is used in the determination of α as described next. The temperature coefficient of resistance (TCR) is determined as a function of temperature for each TPS. R^* and the time correction, t_c, are found from the following equation:

$$R(t) = R^* + A(t - t_c)^{1/2} + B(t - t_c) \tag{7}$$

The t_c value is changed to find the best fit of the data.[25] A, B, and R^* are constants of the equation determined during fitting the data to eq 7.

After applying the time correction, the thermal diffusivity, α, is found by maximizing the fit of the data to $\overline{\Delta T(\tau)}$ versus $H(\tau)$, in an iterative process. Data between $2t_c$ and 0.65θ were used in the evaluation of eq 7 to determine the t_c and R^* values. Data between 0.25θ and 1.30θ were used in the evaluation of thermal diffusivity.

As described previously, the one-sided TPS technique is utilized by adhering the TPS to poly(vinyl chloride) (PVC), which serves as a backing support and partial insulator. Since PVC is not a perfect insulator, the energy from the TPS will be distributed between the PVC and the sample. Finite difference models were developed and used to determine this distribution of energy. The function used to describe the fraction of energy going into the sample was

$$z = a((gR_c - hR_k)^2)^b + dR_k + fR_c \tag{8}$$

where a, b, d, f, g, and h are constants. R_c is the dimensionless volumetric capacity ratio.

$$R_c = \frac{(\rho c_p)_{s'}}{(\rho c_p)_{s'} + (\rho c_p)_{p'}} \tag{9}$$

in which ρ is the density and c_p is the specific heat capacity. The subscript s′ and p′ represent the sample and TPS probe backing material (PVC), respectively. Since

$$\alpha = \frac{k}{\rho c_p} \tag{10}$$

α and k for both the PVC and the sample were used in the analysis. R_k is the sample conductivity ratio.

$$R_k = \frac{k_{s'}}{k_{s'} + k_{p'}} \tag{11}$$

The fraction of energy is applied to the thermal conductivity as

$$k = \frac{2zP_{av}}{4\pi^{1/2}a}\frac{1}{\text{slope}} \tag{12}$$

Since z is a function of the sample k, z is substituted into the calculation of k until consecutively calculated values of k vary insignificantly.

Simulation Methods

This study utilized three water models: the rigid/nonpolarizable SPC/E,[26] TIP4P-Ew,[27] and the rigid/polarizable TIP4P-FQ[28] potentials. The SPC/E and TIP4P-Ew models have fixed hydrogen point charges located at the hydrogen atomic positions and a fixed oxygen charge with respective positions at the oxygen atomic site or displaced 0.125 Å from the oxygen atom along the dipole vector toward the hydrogen atoms. The TIP4P-FQ potential has the hydrogen charges located at the hydrogen sites and the oxygen charge placed 0.15 Å from the oxygen atom along the dipole vector toward the hydrogen atoms. All models possess a Lennard-Jones (LJ) 12-6 interaction site located on the oxygen atom. In addition, a five-site rigid methane model was used, comprising a LJ 12-6 interaction site on the carbon atom and fixed partial charges on the carbon and hydrogen atoms.[29] The TIP4P-FQ potential was used in this study because of its good performance in the prediction of structural and dynamical properties of methane hydrates as compared to flexible and nonpolarizable water potentials.[30] The TIP4P-FQ model has also been used in MD simulations of methane hydrate growth and break-up.[31,32] Although the TIP4P-FQ model only accounts for in-plane water polarizability,[28] it captures the essential physics of hydrates adequately.[30] There are many other polarizable potential models for water,[33−41] but it is beyond the scope of this work to test and validate polarizable water potentials for hydrate MD simulations. The SPC/E and TIP4P-Ew models constitute reparameterizations of the popular SPC[42] and TIP4P[43] potentials and were included in this study to afford a comparison with more widely used models. To corroborate the calculation method for hydrate thermal conductivity, additional estimates were made for ice and liquid water for each potential model.

The computational methodology used in this study was similar to that used previously in equilibrium MD simulations of methane hydrates.[30] The Lekner method[44,45] offers the mathematically definitive solution for electrostatic interactions between point charges in infinitely periodic systems, and this was used to compute these interactions in this study. The technique was implemented using an efficient three-dimensional cubic spline interpolation scheme described previously.[46] The shifted-force formulation for LJ interactions was used with a cut-off radius of 10 Å, and the Lorentz−Berthelot mixing rules were applied for interactions between different types of LJ sites.[47] The multiple time step techniques outlined previously were used, including the tabulation of charge independent terms for TIP4P-FQ water−water and water−methane interactions for use with the Lekner method.[46] This involved calculation of the LJ and minimum image electrostatic interactions at each short time step and the full Lekner interaction at each long step. The outside reference system propagator form (XO-RESPA) was used for multiple time step extended system dynamics.[48] In this explicit reversible integrator, the external reservoir's interaction with the molecular system (e.g., via a thermostat or barostat) is applied at each long time step. In the case of hydrate and liquid water simulations, Anderson−Hoover NPT dynamics were used with isotropic cell fluctuations, while NVT dynamics were applied for simulation of an orthorhombic ice simulation box, using the Martyna−Tuckerman−Klein (MTK) thermostat.[48] The MTK thermostat is implemented in a reversible manner and is similar to the Nosé−Hoover thermostat.[48] The velocity Verlet method was used for all simulations, in a modified form for NPT dynamics.[48] The RATTLE algorithm[49] for bond constraints was utilized. The Verlet algorithm was used to propagate the electronic degrees of freedom in the TIP4P-FQ model. The thermostat and barostat inertia parameters were found by $Q = Xk_BT\tau_Q^2$ and $W = (X + 3)k_BT\tau_B^2$, respectively, where X is the number of degrees of freedom to which the thermostat and barostat were coupled (i.e., the molecular centers of mass).[48] τ_Q and τ_B were set at 100 and 500 fs, respectively. For the TIP4P-FQ temperature associated with the rates of change of charge, the thermostat inertia parameter was found by $Q = Xk_BT\tau_Q^2$, where X is the number of electronic degrees of freedom (i.e., $2N_{water} - 1$).[48] In this case, τ_Q was set to 50 fs, with the set value for the thermostat at 1 K. This constitutes rather mild coupling to the temperature and pressure reservoirs, and some additional production simulations were carried out for comparison in the microcanonical (NVE) ensemble.

The starting crystal configuration was based on the X-ray diffraction analysis of the cubic unit cell of structure I ethylene

oxide hydrate by McMullan and Jeffrey,[50] which provides the positions of the oxygen atoms and the centers of mass of the methane molecules. To investigate if system size has an effect on the thermal conductivity, simulation boxes of $2 \times 2 \times 2$ and $3 \times 3 \times 3$ unit cells were prepared, containing 368 and 1242 water molecules, respectively. The initial orientations of the water molecules were selected in a random manner so as to conform to the Bernal−Fowler rules[51] and so that the total dipole moment of the system would be vanishingly small.[52] The box lengths of the initial configurations were 24.06 and 36.09 Å for the $2 \times 2 \times 2$ and $3 \times 3 \times 3$ unit cell systems, respectively, consistent with the unit cell length of 12.03 Å at 248 K.[50] Having observed no size dependence of the estimate for thermal conductivity or density in hydrate simulations (cf. Results and Discussion), the $5 \times 3 \times 3$ orthorhombic unit cell of Hayward and Reimers[53] was used as a starting configuration for hexagonal ice, containing 360 water molecules in a proton-disordered structure, with a zero net dipole and a zero net quadrupole moment. The *x*, *y*, and *z* box lengths were 22.535, 23.419, and 22.08 Å, respectively, giving a density very close to the experimental value of 920 kg/m^3 at 273 K and ambient pressure.[54] A total of 256 water molecules was used for liquid water simulations.

The number of methane molecules in the systems was set to correspond to 80, 90, and 100% of the maximum theoretical occupation to examine the effect of methane composition on the thermal conductivity and the hydrate system density. For 8-unit cell systems, there were 368 water and 52, 57, or 64 methane molecules for the 80, 90, and 100% occupation cases, respectively. There were 1242 water and 173, 194, or 216 methane molecules present for the 80, 90, and 100% occupation cases, respectively, in the 27-unit cell systems. For partial occupation, methane molecules were removed manually from the fully occupied system in a uniform fashion, so that each portion of a simulation box would have approximately the same local methane composition.

Specific simulations were also carried out for an empty hydrate lattice, to ascertain the extent of its metastability. We employed the geometric hydrate−ice−liquid distinction criteria of Báez and Clancy to distinguish between the hydrate, ice lattices, and liquid phase.[55] These involve the calculation of an angular order parameter to quantify the tetrahedral nature of bonding for nearest-neighbor water molecules, followed by the recognition of five-membered rings of water molecules present in hydrate structures but absent in liquid water and ice. This allows a preliminary classification of hydrate-, ice-, and liquid-like molecules, which is refined further by grouping hydrate-like molecules into clusters and taking into account the identities of neighboring water molecules.[55]

A (1, 4) fs time step structure was used for the 8-unit cell hydrate, ice, and liquid water systems, while a (1.5, 7.5) fs setting was used for 27-unit cell hydrate systems,[46] in which LJ and minimum image electrostatic interactions were computed every 1 or 1.5 fs and a full Lekner evaluation was implemented every 4 or 7.5 fs. The TIP4P-FQ charge masses were set to 6.5×10^{-5} and 15×10^{-5} (ps/e)^2 kcal/mol for the (1, 4) and (1.5, 7.5) fs time step settings, respectively.[28] These time step structures were tested for energy conservation in the NVE ensemble and found to be satisfactory; the percentage relative drift in energy, defined as the ratio of the energy drift (expressed as a linear regression coefficient) to the average kinetic energy during the simulation,[56] was less than 0.08% over 100 ps for all potential models.

The thermal conductivity, *k*, was estimated by integration of the autocorrelation function (ACF) of the heat flux vector, according to the Green−Kubo formula.[15] The heat flux vector $\mathbf{J}(t)$ is defined as:[15,57]

$$\mathbf{J}(t)V = \sum_i \frac{1}{2}[\, m_i \mathbf{v}_i^2 + \boldsymbol{\omega}_i \mathbf{I}_i \boldsymbol{\omega}_i + \sum_j \phi_{ij}]\mathbf{v}_i - \frac{1}{2}\sum_{i,j}[(\mathbf{f}_{ij}\cdot\mathbf{v}_i + \mathbf{t}_{ij}\cdot\boldsymbol{\omega}_i)\mathbf{r}_{ij}] - \sum_{\nu=1}^{2} h_\nu \sum_i \mathbf{v}_{i_\nu} \quad (13)$$

where V and ϕ are the volume of the system and the intermolecular interaction, and the velocity, angular velocity, force, mass, position, molecular moment of intertia, and torque are denoted by $\mathbf{v}$, $\boldsymbol{\omega}$, $\mathbf{f}$, m, $\mathbf{r}$, $\mathbf{I}$ and $\mathbf{t}$, respectively. Therefore, the definition of the heat flux vector contains a kinetic contribution, a potential part, and a term for partial enthalpies (for multicomponent systems). The first two terms are evaluated for all N water and methane molecules (where present) in the system, denoted i (or j).[57] Therefore, it is necessary to use center-of-mass velocities and angular velocities and force and torque terms acting between the centers of mass of molecules i and j. The last enthalpy mixing term is specific to (binary) systems[57] containing methane (i.e., occupied hydrate), and h_ν is the average enthalpy for each species ν.[57] The average enthalpy was found for each species from the sum of the component's averaged potential energy and contributions to the virial pressure.[57] Integration of the ACF of $\mathbf{J}(t)$ gives k

$$k = \frac{V}{3k_B T^2}\int_0^\infty \langle \mathbf{J}(t)\cdot\mathbf{J}(0)\rangle \mathrm{d}t \quad (14)$$

where k_B is Boltzmann's constant. Although this definition of the thermal conductivity is formally for the microcanonical (NVE) ensemble,[47] it has been verified from selected comparative NVE simulations that the mild coupling to the thermostat and barostat used in the NPT simulations means that this formulation remains valid in the NPT case in this work (cf. Results and Discussion).

The heat flux vector was evaluated at each short time step (1 or 1.5 fs time step for the two different time step structures). For hydrates, all computations were carried out at 276 K and at 0.1, 9.5, 15, 30, 50, and 100 MPa. Simulations at 9.5 MPa were carried out for all three water potentials and both 8- and 27-unit cell systems for empty, 80, 90, and 100% occupied systems. At other pressures, simulations were performed for 8-unit cell systems with methane occupations of 80 and 100% using the TIP4P-FQ and SPC/E models, having established that there was no dependence on system size for the density or thermal conductivity (cf. Results and Discussion). The initial X-ray diffraction configurations were equilibrated at 276 K for 100 ps at each pressure and for each potential, and the resultant configurations were used as input for production simulations. These simulations were then carried out for 3−4 ns and between 0.8 and 1 ns for the 8- and 27-unit cell systems, respectively. Five independent hydrate simulations were carried out at each state point for each potential, to define a mean thermal conductivity and to estimate a standard deviation. Various relaxed snapshots of the system from the latter portion of the 100 ps equilibration period were used as input for these runs, with randomized velocities sampled from the Maxwell−Boltzmann distribution. For the 8-unit cell case, additional 10 ns NPT simulations at 276 K and 9.5 MPa were undertaken for each potential to assess the impact of more extensive sampling to define the heat flux ACF. Also, to gauge the validity of thermal conductivity estimates in the NPT ensemble, selected 4 ns NVE runs were performed at densities corresponding to an average pressure of 9.5 MPa (determined by the averaged density obtained from the 4 ns NPT runs at 9.5 MPa).

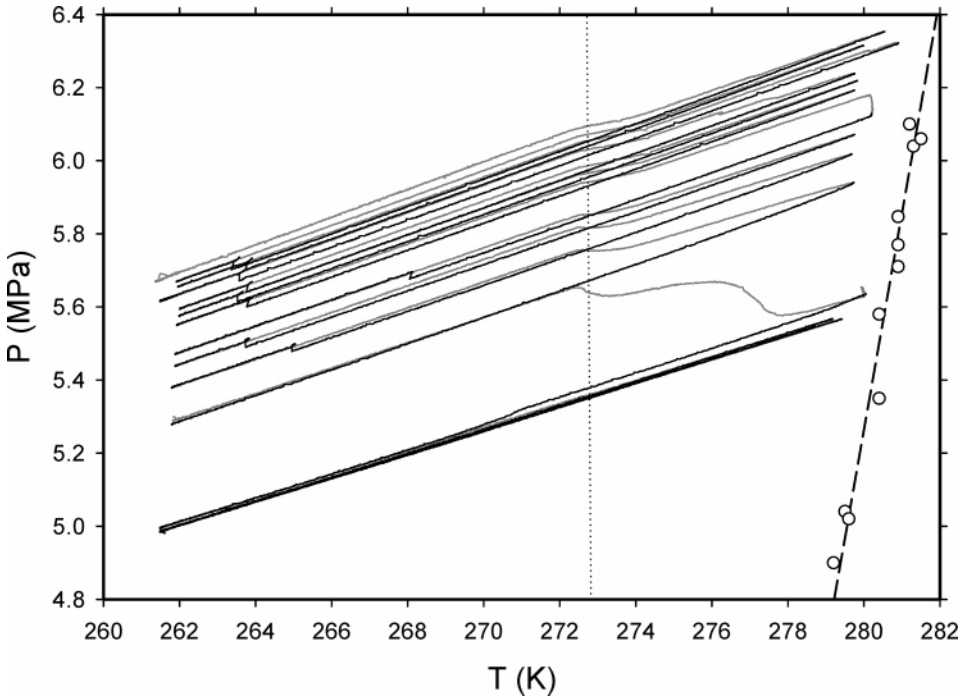

Figure 4. Pressure−temperature history of the hydrate formation phase of the experiment. —: Cooling; gray line: heating; ○: VLH equilibrium data[1]; and ·····: melting point of ice as a function of pressure.

For ice, the initial orthorhombic configuration (with a density of 924 kg/m^3) was relaxed at 273 K in the NVT ensemble for 100 ps for each potential, followed by 1.5 ns production runs. In an effort to estimate the ice thermal conductivity at the density corresponding approximately to zero mean (i.e., ambient) pressure for each potential at 273 K, short NPT runs were carried out for around 20 ps, in which the ratios of the *x*, *y*, and *z* box lengths were kept fixed. Using this rescaled orthorhombic simulation box as a starting point, up to 12 NVT runs of around 50 ps duration were performed by altering the initial density slightly while keeping a fixed ratio of box lengths, and the relaxation of the mean pressure was monitored. Once a given density was found to produce a mean pressure of around zero, a 1.5 ns NVT production run was then performed, using the relaxed configuration as input. For liquid water, NPT simulations of around 3 ns duration were carried out at 298 K and 101.3 kPa, and the experimental thermal conductivity was found from the IAPWS correlation at those conditions.[58] For both water and ice, five independent NPT or NVT simulations were carried out to define a mean thermal conductivity and to estimate the standard deviation.

In all cases, the ACF of the heat flux vector was computed for at least 20 ps, based on the evaluations of the heat flux vector at every short time step for the entire duration of the production run. In the hydrate case, validation that the estimate of the thermal conductivity had converged within the 20 ps time scale was carried out using longer definitions of the ACF from the same simulation (albeit with a necessarily lower sampling ratio, vide infra).

Results and Discussion

Experimental. Formation of the methane hydrate sample in the HTMD was monitored by recording the pressure as the temperature of the sample was varied above and below the freezing point of water. The pressure and temperature data recorded during hydrate formation in the HTMD are contained in Figure 4 along with the three-phase, vapor-liquid-hydrate (VLH) equilibrium data for methane hydrate from the literature.[1] Methane hydrate is stable at conditions to the left of the line describing the literature data. The temperature of the sample in the HTMD was always kept within this region of hydrate stability.

Initially, hydrate formation proceeded slowly, likely occurring at the interface of water and gas in the sample cup. The formation of ice was evident in the first 10 cooling cycles by the small rise in pressure. Some hydrate formation was also observed as the temperature approached freezing during the heating cycles. Following the heating phase of cycle 7, which ended at about 280.2 K and 6.17 MPa, the system was allowed to remain at this temperature for about 9 h. Additional hydrate continued to form during this interval. After this, several more cycles were performed at 1 K/h. During the 11th heating cycle, a large amount of hydrate formation was observed. A small amount of additional hydrate formation was evident in the next cooling cycle; however, in the last three cycles (13−15), no additional hydrate or ice formation was evident in the pressure data. The total pressure drop corresponded to the amount of gas uptake anticipated for complete conversion of the water to hydrate.

The sample of hydrate in the cup assembly was then compacted using the internal piston to push on the cup top. The thermal conductivity of the sample during the initial compaction and during several subsequent cycles of releasing and reapplying the compaction pressure are shown in Figure 5. The initial compaction was performed at 261.5 ± 0.1 K under a methane pressure of 4.79 ± 0.11 MPa. Three cycles of releasing and reapplying the compaction pressure were then performed. Data obtained during the first two cycles are shown in Figure 5 and are in Table S1 of the Supporting Information. The sample temperature was then raised to slightly above the melting point of water, and the compaction pressure was lowered and raised again. The thermal conductivity value did not change, as shown by the data point in Figure 5 taken at 275.4 K at a compaction pressure of 26.9 MPa and a gas-phase pressure of 4.6 MPa.

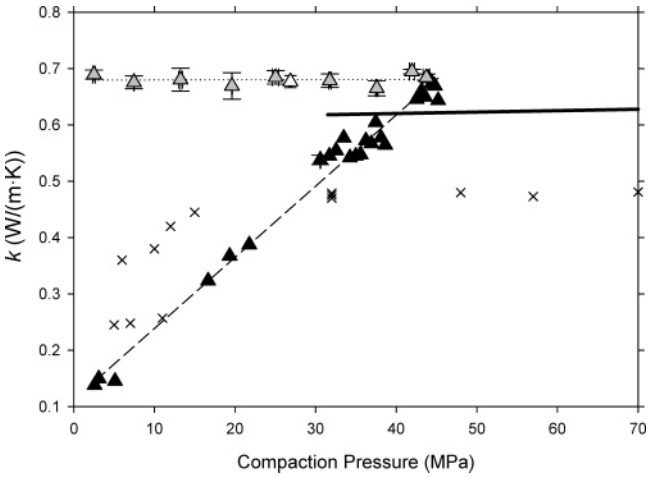

Figure 5. Thermal conductivity of methane hydrate as a function of compaction pressure. ▲: NETL data during initial compaction at 261.5 K; gray triangle: NETL data during several cycles of releasing and applying compaction pressure at 261.5 K; △: NETL data at 275.4 K; ×: USGS data published by Waite et al.[7]; and —: USGS data correlation published by Waite et al.[2]

This indicates that the presence of ice did not influence the measurements. A weak positive trend with compaction pressure was also observed. The average thermal conductivity of the compacted sample was 0.68 ± 0.01 W/(m·K) at an average methane gas pressure of 4.67 ± 0.005 MPa. The slope and intercept of the regression shown for the compacted sample are 2.70×10^{-5} and 0.679, respectively.

Also shown in Figure 5 are previous data by Waite et al.[7] for radial compaction pressures up to 70 MPa for methane hydrate prepared from granular ice according to a method described by Stern et al.[59,60] As this sample was being compacted, the compaction pressure dropped from about 11 MPa down to about 6 MPa, likely due to a shift in the hydrate grains during compaction.[7] They have more recently repeated their experiment[2] at higher radial compaction pressures (102 MPa) and with modifications to their equipment to permit more uniform compaction of the hydrate sample.[61] This resulted in their more recent thermal conductivity results being higher than their previous ones. The maximum thermal conductivity from our work is slightly higher than their most recent values, possibly indicating that even at 102 MPa, their sample was still slightly more porous than ours. The correlation of thermal conductivity with compaction pressure also has a slightly higher slope than our data that could also be due to more residual porosity in their sample.

Figure 6 and Table S2 in the Supporting Information contain thermal conductivity data for the compacted methane hydrate as a function of temperature. The individual data points making up the average values shown in this figure were taken over a methane gas pressure range of 4.6−6.3 MPa and at a range of compaction pressures up to 43.7 MPa. Also shown are data correlations published by Waite et al.[2,7] and the data obtained by Huang and Fan using a double-sided TPS technique.[8] The recent data of Waite et al.[2] were taken at a confining pressure of 31.5 MPa after compaction at 102 MPa, whereas their earlier data were taken on a sample that was compacted to 70 MPa.[7] Huang and Fan[8] also used a 0.971 mol/m^3 solution of aqueous sodium dodecyl sulfate to enhance the packing of the hydrate during its formation.[62] They also applied a compaction pressure of 2 MPa to their sample after formation. Figure 6 shows that their results are lower than ours and the recent results of Waite et al.;[2] however, they are higher than the earlier results of Waite et al.[7] Our results in Figure 6 and those of Waite et al.[2,7] have the same slight negative trend with temperature. Unlike this trend, the slope of Huang and Fan's data[8] is positive, possibly from any water−surfactant solution trapped in the samples, as the thermal conductivity of water has a positive temperature dependence (Figure 3). The average thermal conductivity of our data in Figure 6 was 0.68 ± 0.01 W/(m·K). The slope and intercept of the regression shown for the compacted sample are -1.91×10^{-4} and 0.7345, respectively.

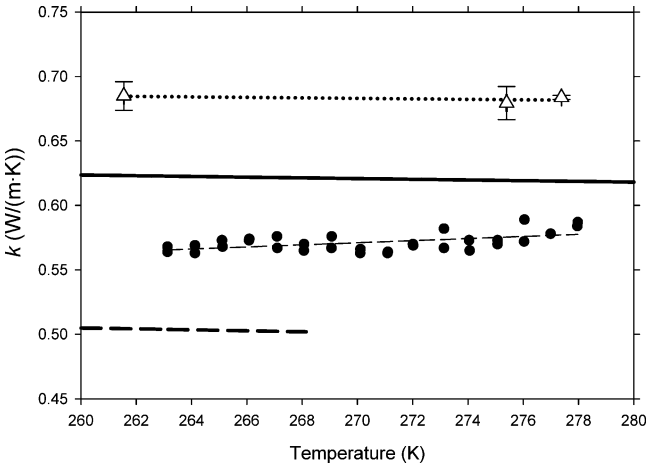

Figure 6. Thermal conductivity data as a function of temperature. △: NETL; —: correlation of Waite et al.[2]; - - -: correlation of Waite et al.[7]; and ●: Huang and Fan.[8]

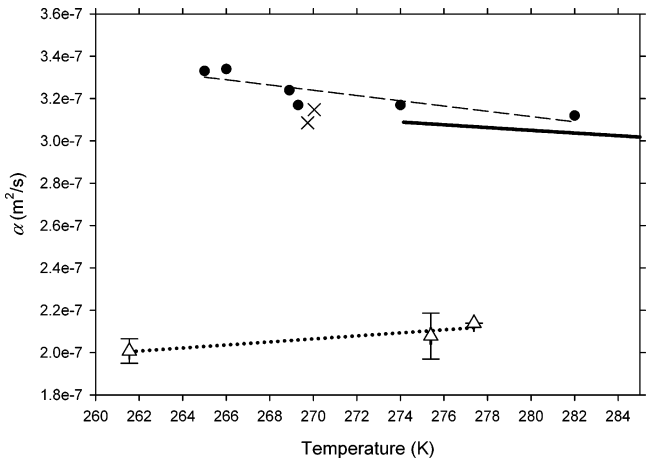

Figure 7. Thermal diffusivity as a function of temperature for methane hydrate samples. △: NETL, compacted sample; ×: deMartin,[6] compacted sample; —: from a correlation by Waite et al.,[2] compacted sample;[2] and ●: Kumar et al.,[11] uncompacted sample.

The TPS technique also permits the simultaneous determination of thermal diffusivity as described previously. The thermal diffusivity data as a function of temperature obtained in our experiments for compacted methane hydrate are shown in Figure 7 and contained in Table S2 of the Supporting Information. Also shown are the available literature data for thermal diffusivity of porous and compacted methane hydrate in the temperature range near 273 K.[2,6,11] Our results for compacted methane hydrate are lower than those obtained by others. This may be due to the manner in which the samples were formed and to differences in the experimental techniques. The data of others were determined on samples similarly prepared from granular ice, whereas our samples were prepared from a small sample of water that was repeatedly cooled and warmed under methane pressure. deMartin noted that his sample appeared to contain water ice that could have influenced his

results.[6] We have recently performed finite difference modeling on the single-sided TPS technique with PVC as the support material. The results indicate that measured values of thermal diffusivity will tend to be lower than actual values when a sample has a higher thermal diffusivity value relative to PVC, such as methane hydrate. Additional work to better define the thermal diffusivity of compacted methane hydrate using the single-sided TPS technique is being pursued at NETL.

Thermal Conductivity Simulations. As an initial validation of the quality of the potential models and of the equilibrium MD method for the prediction of thermal conductivity, the values for ice at 273 K were estimated. The melting points of TIP4P-FQ, SPC/E, and TIP4P-Ew ice have been reported recently as 303 ± 8,[63] 215,[64] and 245 K,[64] respectively, using NPT simulation and Ewald electrostatics. However, the ice remained kinetically stable during the 1.5 ns runs at 273 K and at each density, judged by the Báez and Clancy criteria and the steady value of the potential energy. The densities for which the mean pressures were approximately zero at 273 K were 971, 949, and 938 kg/m^3 for the TIP4P-FQ, SPC/E, and TIP4P-Ew models, respectively. This is in good agreement with previously reported respective values of 968,[65] 950,[64] and 936 kg/m^3,[64] obtained using Parrinello−Rahman NPT simulation[66] with Ewald electrostatics. The TIP4P-FQ dipole moment distribution was 3.08 ± 0.14 D at this density, in accord with a reported value of 3.10 ± 0.15 D.[65] Conversely, the dipole moments of the fixed charge SPC/E and TIP4P-Ew models remain at their respective monomer values of 2.35 and 2.20 D (ref 67) in ice, ipso facto. The TIP4P-FQ density is largest, followed by the SPC/E and then the TIP4P-Ew models, and all are larger than the experimental value of 920 kg/m^3.[54]

The relative differences in the ice densities for the three different models may be rationalized qualitatively by the extent of hydrogen bonding and by the magnitude of the dipole moment. In the case of pure liquid water at 275 K, the average number of hydrogen bonds per water molecule was found to be 3.70, 3.61, and 3.67 by a geometric definition for the TIP4P-FQ, SPC/E, and TIP4P-Ew models, respectively, while the respective molecular dipole moments were 2.69 ± 0.2, 2.35, and 2.20 D (i.e., the monomer values for the latter two).[67] The greater extent of hydrogen bonding and the larger dipole moment in the TIP4P-FQ potential lead to a lower system volume (and a higher density) relative to the nonpolarizable potentials. Although the SPC/E model has fewer hydrogen bonds per molecule (3.61) than the TIP4P-Ew potential (3.67) for pure water at 275 K, the dipole moment is still larger for the SPC/E potential,[67] enhancing the relative strength of hydrogen bonding and leading to a greater contraction in system volume relative to the TIP4P-Ew model. These observations for pure water help to explain this trend observed in the results for ice.

The results for the ice thermal conductivity were 2.422 ± 0.042, 1.731 ± 0.034, and 1.838 ± 0.033 W/(m·K) for the TIP4P-FQ, SPC/E, and TIP4P-Ew potentials, respectively, at the densities for which their mean pressures were approximately zero. The mean thermal conductivities and standard deviations were defined based on five independent simulations, using ACFs of 20 ps in duration. For each simulation, the results were consistent after 1 and 1.5 ns of simulation, so it was concluded that the simulations were of sufficient duration. At a constant density of 924 kg/m^3, close to an experimental density of 920 kg/m^3,[54] the respective results were 2.483 ± 0.050, 1.802 ± 0.039, and 1.884 ± 0.031 W/(m·K). Therefore, as found in the case of the hydrate results (vide infra), changes in density have a relatively weak effect on the measured thermal conductivities. The experimental value at 273 K is approximately 2.2 W/(m·K).[68,69] The TIP4P-FQ result is in slightly better agreement with the experimental value, being some 10% larger, although the SPC/E and TIP4P-Ew results are less than 20% smaller.

It is interesting to note that the TIP4P-FQ model yields a larger thermal conductivity than the nonpolarizable models for ice. The greater propensity for the formation of stronger hydrogen bonds for the TIP4P-FQ model, especially in the ice or hydrate state where the molecular dipole moment is enhanced relative to liquid water, tends to increase the thermal conductivity. In real ice or hydrate samples, there will be some structural defects present, even if a high degree of compaction has been applied to minimize porosity. The crystal structures used in the molecular simulations contain no porosity or structural defects that would serve to decrease the efficiency with which phonons conduct thermal energy in the host lattice. Therefore, one would expect molecular simulations to result in artificially higher values for the thermal conductivity as compared to experiments. This is a limitation of the relatively small system sizes that can be investigated with atomistic modeling. It would be necessary to carry out many simulations with varying geometry and extent of defects and porosity to assess quantitatively the degree to which the thermal conductivity would be reduced by the presence of defects. Bearing this in mind, the lower results of SPC/E and TIP4P-Ew for ice relative to experiment show that these models are less accurate than TIP4P-FQ in this regard.

Estimation of the thermal conductivity of pure liquid water acts as an additional validation exercise. The IAPWS correlation value for the thermal conductivity at 298 K and 100 kPa is 0.61 W/(m·K).[58] The simulation results were 0.673 ± 0.027, 0.724 ± 0.018, and 0.743 ± 0.017 W/(m·K) for the TIP4P-FQ, SPC/E, and TIP4P-Ew potentials, respectively, gauged from five independent simulations using ACFs of 20 ps duration. The TIP4P-FQ result is in the best agreement with the experimental value, being some 10% larger. The TIP4P-FQ model leads to a lower thermal conductivity than the nonpolarizable models in the liquid state, in contrast to the hydrate and ice results where it gives the highest values of the models tested (see the following discussion for hydrate results). This may be rationalized by both slower rotational and translational modes[70] for TIP4P-FQ water. The hydrogen bond breakage and reformation kinetics are slower in TIP4P-FQ water, with hydrogen bond relaxation times of 5.12 ± 0.04, 4.87 ± 0.03, and 4.35 ± 0.02 ps for the TIP4P-FQ, TIP4P-Ew, and SPC/E models, respectively, at 298 K with Lekner electrostatics.[67] Similarly, a slower translational motion in TIP4P-FQ water is characterized by self-diffusion coefficients of 2.11 ± 0.1, 2.29 ± 0.15, and 2.42 ± 0.15 × 10^{-9} m^2/s for the TIP4P-FQ, TIP4P-Ew, and SPC/E potentials, respectively, for the same conditions.[67] As discussed earlier, the different degree of TIP4P-FQ polarization in the homogeneous environment of pure water relative to the solid state appears to result in qualitatively different behavior, confirming again the important role of polarizability in water physics.

In an MD study of thermal conductivity, Ohara reported an estimate of 0.95 W/(m·K) for pure water in the 300−320 K temperature range, using the SPC/E model in conjunction with a nonequilibrium technique, without the use of long-range electrostatics.[70] This result is about 30% larger than the value of 0.72 ± 0.02 W/(m·K) predicted using the SPC/E potential in this study. Here, the heat flux vector was defined after 2 and 3 ns of simulation, in addition to after 4 ns at the end of the simulation, and similar results were obtained for the thermal conductivity. It is possible that the difference between the SPC/E result of this study and that of Ohara is attributable to the use

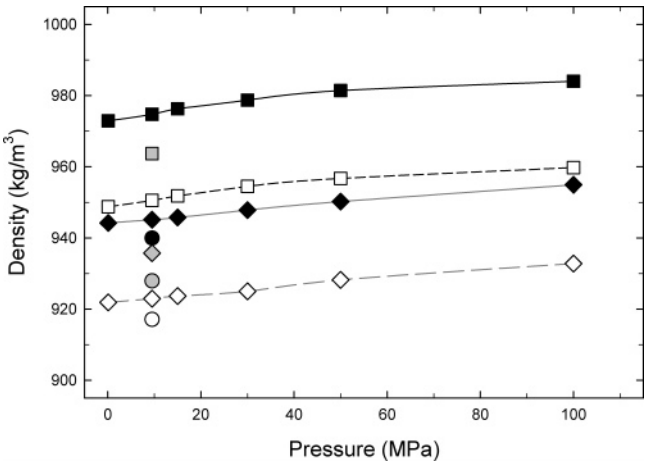

Figure 8. Calculated densities for occupied 8-unit cell hydrate systems. TIP4P-FQ: −■−: 100% occupied; gray box: 90%; and −□−: 80%. TIP4P-Ew: ●: 100%; gray circle: 90%; and ○: 80%. SPC/E: −◆−: 100%; gray diamond: 90%; and −◇−: 80%.

of different estimation techniques (i.e., equilibrium and non-equilibrium simulation) or perhaps to the omission of long-range electrostatics.

The calculated densities for the occupied 8-unit cell hydrate systems are presented in Figure 8 and in Table S3 of the Supporting Information. The densities of the TIP4P-FQ systems are about 3% higher than those of the SPC/E case, for the same composition, while the TIP4P-Ew densities are about 0.6% lower than the corresponding SPC/E values. For all potential models, the densities of the 80% occupied systems are about 2.5% smaller than those of the 100% occupied case. Ideal behavior, assuming no change in the lattice parameters, is for the 80% occupied lattice to have a density of 2.7% less than the 100% occupied lattice. Thus, the observed 2.5% difference in densities means that the lattice parameters for the 80% occupied system are very close to those for the 100% occupied case; this can be seen in Table S4 of the Supporting Information. The empty cavities in the partially occupied systems remain stable for the duration of the simulation, and the system volume decreases little in comparison to the fully occupied case. It can be seen that the density does not increase greatly as the pressure increases from atmospheric to 100 MPa. For instance, the density of the TIP4P-FQ system increases from 973 to 984 kg/m^3 over this range. Therefore, the increasing pressure does not cause the hydrate lattice structure to distort significantly, even in the case of the empty cavities, for 80% methane occupations. Reference to Table S4 (Supporting Information) shows that the TIP4P-FQ lattice parameter declines by 0.38 and 0.25% from 0.1 to 100 MPa for 80 and 100% occupation, respectively, while the corresponding respective results for the SPC/E model are 0.38 and 0.42%.

The relative differences in the hydrate densities for the three different models may be rationalized qualitatively by the extent of hydrogen bonding and by the magnitude of the dipole moment, in a similar way to the results for ice. The anisotropic environment of the hydrate state accentuates the TIP4P-FQ dipole moment and charge polarization relative to the isotropic liquid state. In the hydrate state at 276 K, the molecular dipole moment distribution of the TIP4P-FQ water molecules is enhanced over the liquid value of 2.69 ± 0.2 D (at 275 K) to values of 3.02 ± 0.15 and 3.04 ± 0.14 D for pressures of 0.1 and 100 MPa, respectively. The SPC/E and TIP4P-Ew dipole moments remain at their respective monomer values of 2.35 and 2.20 D[67] in the hydrate state. The greater extent of hydrogen

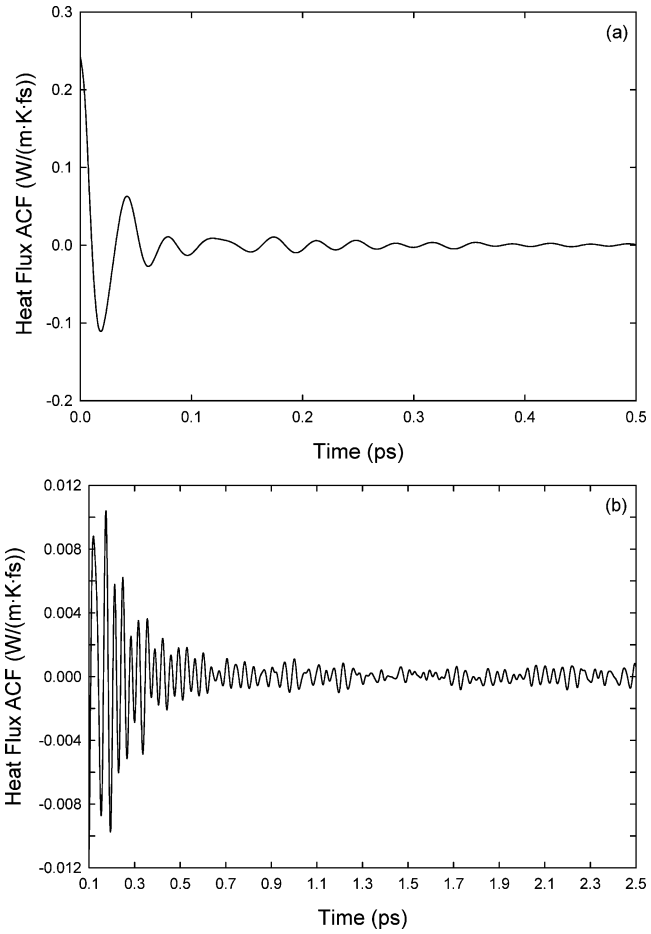

Figure 9. Heat flux ACF of 8-unit cell SPC/E hydrate system at 276 K and 9.5 MPa at 100% occupation after 1 ns. (a) 0−0.5 ps and (b) 0.1−2.5 ps.

bonding and the larger dipole moment in the TIP4P-FQ potential results in a lower system volume (and a higher density) relative to the nonpolarizable potentials.

The results for the system density were in agreement for the 8- and 27-unit cell hydrate systems, at 9.5 MPa; the use of long-range electrostatics renders the 8-unit cell system size adequate for prediction of equilibrium properties. Simulations of empty lattices were carried out for both system sizes at a pressure of 9.5 MPa. For the TIP4P-Ew model, these structures were stable for the duration of the simulation (4 and 1 ns for the 8- and 27-unit cell systems, respectively), while the lattice structure started to dissociate for the SPC/E and TIP4P-FQ potentials after about 0.75 and 0.5 ns, respectively. The break-up took place earlier for the 27-unit cell systems, after about 0.6 and 0.4 ns for the SPC/E and TIP4P-FQ models, respectively. The extent of dissociation was monitored quantitatively using the Báez and Clancy geometric criteria[55] and occurred over periods of 50−150 ps. It is interesting to note that the potentials with the most pronounced hydrogen bonding exhibit the least stability for the empty lattice. The absence of methane molecules in the cavities removes the stabilizing influence of the guest−water van der Waals interactions, which is required to a greater degree for stability in a host lattice composed of more dipolar water molecules.

As a typical example of the ACFs of the heat flux vector, the one for the SPC/E potential in the fully occupied 8-unit cell hydrate system at 9.5 MPa over the first 0.5 ps and from 0.1 to 2.5 ps is depicted in Figure 9a,b, respectively. The ACF was calculated up to 20 ps, based on a 4 ns production

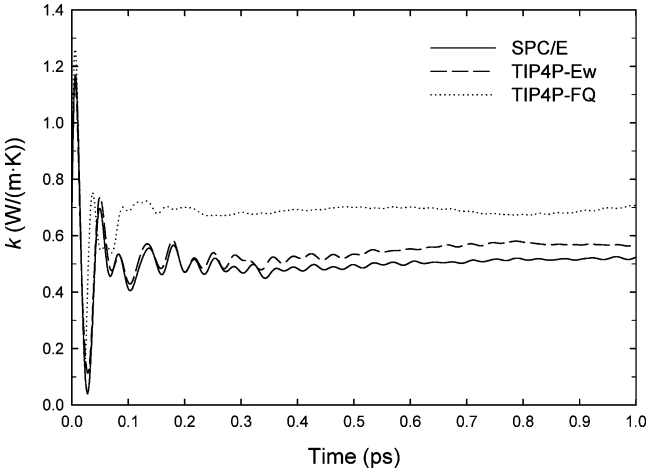

Figure 10. Convergence of a thermal conductivity estimate for 8-unit cell hydrate systems at 276 K for 100% occupation.

simulation, one of five independent simulations. The ACF exhibits rapid fluctuations and decays to zero at long times. It is evident that the amplitude of the successive peaks and troughs decays slowly (Figure 9a,b). The ACF was integrated numerically using Romberg quadrature in conjunction with smooth cubic spline interpolation to generate the required artificial ACF values in between the sampling intervals of 1 or 1.5 fs.[71] The evolution of the estimate for the thermal conductivity is illustrated in Figure 10 for all three water potentials for the same system as shown in Figure 9. Although the integration of the ACF was performed for the whole 20 ps, it is evident that the estimate for the thermal conductivity converges within about 1 ps. No significant differences were observed between the 8- and the 27-unit cell systems. Estimates of the thermal conductivity obtained at earlier points in the MD simulations (after 1, 2, and 3 ns for the 8-unit cells and 0.25, 0.5, and 0.75 ns in the case of the 27-unit cells) were almost identical, indicating that the simulations were of sufficient length to obtain accurate results.

The estimates for the hydrate thermal conductivity from molecular simulation are depicted in Figure 11a for the three potentials as a function of the system pressure for 80, 90, and 100% methane occupations, along with their standard deviations. In this case, the averages and standard deviations have been defined over five independent simulations for each potential, occupation, and state point, using ACFs of 20 ps duration. The simulation results are also given in Table S5 of the Supporting Information. Figure 11b shows the same data along with the experimental results for the compacted samples and corresponding standard deviations in the pressure range of 0−15 MPa. The experimental data are contained in Table S6 of the Supporting Information. The experimental pressures represent methane pressures that were varied while the sample was maintained under a slight compaction pressure to ensure contact of the sample with the sensor. The values shown are for the compacted sample that had been consolidated as described earlier. Similar to the results presented in Figures 6 and 7, the average of the experimental thermal conductivity data presented in Figure 11b is 0.68 ± 0.01 W/(m·K).

To gauge the effect of integration over longer ACFs on the convergence of the estimate for the thermal conductivity, ACFs with lengths of 20, 50, and 100 ps were defined from the set of 4 ns runs for 8-unit cell systems for each potential and state point. This led to simulation/ACF sampling ratios of 400:1, 80:1, and 40:1, respectively. In accord with the relatively rapid convergence of the estimate in the examples of Figure 9b, it

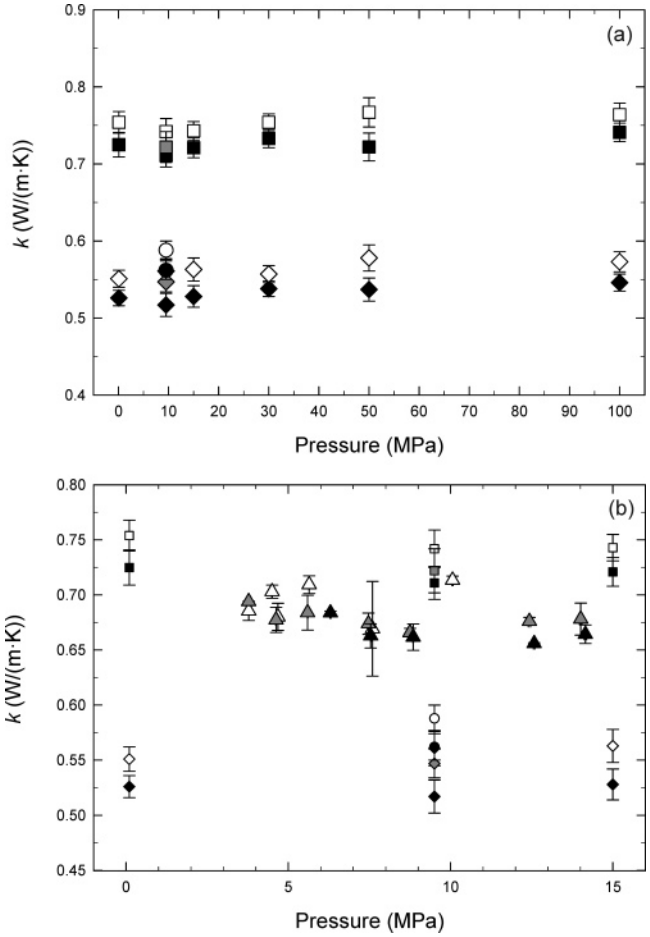

Figure 11. Thermal conductivity results as a function of pressure. (a) Simulation results from 0.1 to 100 MPa; symbols same as in Figure 8. (b) Experimental and simulation results compared over the range of experimental pressures used. Simulation symbols same as in Figure 8. Experimental data: △: 262 K; gray triangle: 275 K; and ▲: 277 K.

was found that these different ACF lengths led to almost identical results, well within the respective standard deviations. Additional 10 ns NPT simulations were carried out for the three potentials at 9.5 MPa and 276 K to allow for the definition of 20, 100, and 250 ps length ACFs (i.e., with respective sampling ratios of 500:1, 100:1, and 40:1), but the results for the thermal conductivity estimate were almost identical.

Five independent NVE simulations were carried out for each potential at densities of 974.7, 945.1, and 939.9 kg/m^3, for the TIP4P-FQ, SPC/E, and TIP4P-Ew models, respectively. From earlier results, these densities correspond to average pressures of around 9.5 MPa. Using NPT configurations as input, the pressure and temperature remained stable in these simulations. The average and standard deviation results were 0.706 ± 0.017, 0.522 ± 0.017, and 0.558 ± 0.014 W/(m·K) for the TIP4P-FQ, SPC/E, and TIP4P-Ew potentials, respectively, which is in agreement with the NPT results at this temperature and pressure (cf. Table S5 in the Supporting Information).

It can be seen that the estimates using the TIP4P-FQ model of 0.71−0.77 W/(m·K) over the pressure and composition range are in reasonable agreement with the experimental results, while those of the SPC/E and TIP4P-Ew potential are some 20−30% lower. As was the case for the system density, the results for the thermal conductivity were in agreement for the 8- and 27-unit cell systems, at 9.5 MPa. The thermal conductivities of the 80% occupied systems are slightly higher than those of the fully occupied systems. The increase in k with decreasing

occupation of the hydrate cages is consistent with the idea that phonon scattering due to the guest molecules is responsible for the unusually low thermal conductivity of methane hydrate.[14−18] However, the overlapping of standard deviation bars makes any definitive conclusion about the dependence of *k* on occupation difficult. Nevertheless, the thermal conductivity is not a strong function of the occupation of the hydrate guest sites in the range of 80−100% occupation. In addition, there does not appear to be any trend of increasing thermal conductivity with higher pressure in either the experimental or the simulation results.

As noted previously, the SPC/E and TIP4P-Ew thermal conductivity predictions of 0.52−0.59 W/(m·K) are in poorer agreement with the experimental results over the pressure and composition range than those of the TIP4P-FQ potential. The greater propensity for the formation of stronger hydrogen bonds for the TIP4P-FQ model, especially in the hydrate state where the molecular dipole moment is enhanced relative to liquid water, as noted previously, tends to increase the thermal conductivity. Although the density of the hydrate system predicted by the TIP4P-Ew model is about 0.6% lower than that of the SPC/E potential (cf. Figure 8 and Table S3 of the Supporting Information), the predictions for the thermal conductivity by the TIP4P-Ew model are some 5% higher than those of the SPC/E potential at 9.5 MPa, although the overlapping of standard deviation bars in Figure 11a for the thermal conductivity estimates renders this observation tentative. As mentioned earlier, the inclination of the TIP4P-Ew model to form a greater number of hydrogen bonds may explain the higher thermal conductivity relative to the SPC/E potential. It would appear that the polarizability of the TIP4P-FQ model is an important physical feature, especially in the heterogeneous environment of the hydrate crystal, and this affords a more accurate prediction of the thermal conductivity. This finding agrees with the conclusions of earlier work on equilibrium properties of methane hydrates.[30]

The computed values of 0.52 ± 0.015 and 0.56 ± 0.015 W/(m· K) for the thermal conductivity of fully occupied hydrate at 9.5 MPa using the SPC/E and TIP4P-Ew models are in reasonable agreement with the value of 0.52 W/(m·K) for xenon hydrate at 260 K reported by Inoue et al.[15] The latter result was found by using the TIP4P water model and the same equilibrium technique to calculate the thermal conductivity based on the ACF of the heat flux vector. However, the interaction potentials were truncated smoothly at 8.665 Å, with no long-range corrections applied.[15] Furthermore, substantial differences in the estimates for the thermal conductivity were observed between equilibrium and nonequilibrium estimation techniques.[15]

Conclusion

The thermal properties of a compacted methane hydrate sample have been determined and compared to the reported values in the literature. For thermal conductivity, our measurements and those of Waite et al.[2] indicate that the thermal conductivity should be higher than previously reported values. Our result of 0.68 ± 0.01 W/(m·K), over the temperature range of 261.5−277.4 K, is slightly higher than the average value of 0.62 ± 0.02 W/(m·K) determined from the recently published correlation of Waite et al.[2] over approximately the same temperature range. Molecular dynamics simulations have been performed to calculate the thermal conductivity of a defect-free methane hydrate crystal at 276 K over a methane occupation range of 80−100% and a range of pressures. The average thermal conductivity value obtained with the TIP4P-FQ model was 0.74 ± 0.02 W/(m·K). The use of the higher experimental value for thermal conductivity of low-porosity methane hydrate in reservoir production or climate change simulations appears to be warranted. Similar conclusions regarding the thermal diffusivity of compacted methane hydrate cannot be made. The single-sided TPS values are lower than the few published literature values. Further refinement of the single-sided TPS technique is in progress at NETL to address this issue. The thermal diffusivity values of Waite et al.[2] should be used for compacted methane hydrate.

As compared to the more traditional needle probe and double-sided TPS techniques, the single-sided TPS technique is more conducive to adaptation for field use in hydrate-containing sediments and similar situations where sample penetration and/or immersion of the sensor would be difficult. Potential advantages of the single-sided TPS technique are that the sensor only has to be pressed against the sample, sample disturbance is minimal, and that it facilitates any subsequent analysis of the sample that was in contact with the sensor.

With respect to the molecular simulations, the results for the density and thermal conductivity were consistent for the 2 × 2 × 2 and 3 × 3 × 3 unit cell systems, indicating that the use of long-range electrostatics renders the 2 × 2 × 2 unit cell system size adequate for the prediction of equilibrium properties. It was found that the density did not increase significantly over the pressure range from ambient to 100 MPa. Decreasing methane occupation of the hydrate appears to result in a slight increase in the thermal conductivity over the range of 80−100% occupation. The computed thermal conductivities were virtually independent of pressure over the pressure range studied. The results for the thermal conductivity were 20−30% higher for the polarizable TIP4P-FQ model than for the nonpolarizable SPC/E and TIP4P-Ew potentials and were in better agreement with the experimental results, given that some degree of overestimation would be expected for nonporous, defect-free lattices used in molecular simulation. The quality of the potential models, in addition to the validity of the equilibrium estimation technique for the thermal conductivity, were assessed by comparison of molecular simulation predictions for ice and pure water, and reasonable agreement was obtained with experimental results, especially for the TIP4P-FQ model. It would appear from observations of this study, and from previous work,[30,46,67] that polarizability is an important aspect of water potential models, especially in the inhomogeneous environment of hydrates.

Although compaction of the hydrate samples reduced the porosity to the lowest possible level attainable with the experimental apparatus, the structural defects present in real samples were not taken into account in the molecular simulations, and it is unknown to what extent the inclusion of defects would affect the molecular simulation findings. This would represent a considerable future challenge for molecular simulation, as the geometry of the systems would have to be prepared very carefully, and very large systems would be required.

Acknowledgment. N.J.E. acknowledges useful discussions with Drs. Dan Sorescu (DOE-NETL), Kenneth Jordan (University of Pittsburgh), and Bernhardt Trout (MIT) on the molecular physics of hydrate thermodynamics and quality of water potential models. E.J.R. and N.J.E. performed this work under Contract DE-AM26-04NT41817, subtask 41817.660.01.03 in support of the National Energy Technology Laboratory's Office of Research and Development. The participation of J.K.J. and D.W.S. was supported by NETL through the ORISE Faculty Research Participation Program.

Supporting Information Available: Tables containing thermal conductivity and thermal diffusivity results, density results, and lattice parameters. This material is available free of charge via the Internet at http://pubs.acs.org.

References and Notes

(1) Sloan, E. D., Jr. *Clathrate Hydrates of Natural Gases, Second Edition, Revised and Expanded*; Marcel Dekker, Inc.: New York, 1998.

(2) Waite, W. F.; Stern, L. A.; Kirby, S. H.; Winters, W. J.; Mason, D. H. *Geophys. J. Int.* **2007**, *169*, 767.

(3) Boswell, R. *J. Pet. Sci. Eng.* **2007**, *56*, 9.

(4) Rosenberg, N.; Durham, W.; Kirby, S.; Brewer, P. *Final Report for the September 2001 Workshop on Physical and Chemical Property Measurements for the Gas Hydrate R & D Community*; October 2001. http://www.llnl.gov/tid/lof/documents/pdf/244383.pdf (accessed 9/24/2007).

(5) Gupta, A.; Kneafsey, T. J.; Moridis, G. J.; Seol, Y.; Kowalsky, M. B.; Sloan, E. D. *J. Phys. Chem. B* **2006**, *110*, 16384.

(6) deMartin, B. J. Laboratory Measurements of the Thermal Conductivity and Thermal Diffusivity of Methane Hydrate at Simulated in Situ Conditions. M.S. Thesis, Georgia Institute of Technology, 2001.

(7) Waite, W. F.; Pinkston, J.; Kirby, S. H. *Preliminary Laboratory Thermal Conductivity Measurements in Pure Methane Hydrate and Methane Hydrate−Sediment Mixtures: A Progress Report*; Fourth International Conference on Gas Hydrates: Yokohama, Japan, 2002.

(8) Huang, D.; Fan, S. *J. Chem. Eng. Data* **2004**, *49*, 1479.

(9) Gustafsson, S. E. *Rev. Sci. Instrum.* **1991**, *62*, 797.

(10) Gustafsson, S. E. *Device for Measuring Thermal Properties of a Test Substance—The Transient Plane Source (TPS) Method*; G01N 025/18 ed.; Thermetrol AB (SE): U.S. Patent 5,044,767, Sept. 3, 1991.

(11) Kumar, P.; Turner, D.; Sloan, E. D. *J. Geophys. Res.* **2004**, *109*, 8.

(12) Turner, D. J.; Kumar, P.; Sloan, E. D. *Int. J. Thermophys.* **2005**, *26*, 1681.

(13) Tse, J. S.; White, M. A. *J. Phys. Chem.* **1988**, *92*, 5006.

(14) Tse, J. S. *J. Inclusion Phenom. Macrocyclic Chem.* **1994**, *17*, 259.

(15) Inoue, R.; Tanaka, H.; Nakanishi, K. *J. Chem. Phys.* **1996**, *104*, 9569.

(16) Tse, J. S.; Ratcliffe, C. I.; Powell, B. M.; Sears, V. F.; Handa, Y. P. *J. Phys. Chem. A* **1997**, *101*, 4491.

(17) Tse, J. S.; Shpakov, V. P.; Murashov, V. V.; Belosludov, V. R. *J. Chem. Phys.* **1997**, *107*, 9271.

(18) Tse, J. S.; Shpakov, V. P.; Belosludov, V. R.; Trouw, F.; Handa, Y. P.; Press, W. *Europhys. Lett.* **2001**, *54*, 354.

(19) MacDonald, G. J. *Ann. Rev. Energy* **1990**, *15*, 53.

(20) Kvenvolden, K. A. *Chem. Geol.* **1988**, *71*, 41.

(21) Warzinski, R. P.; Lynn, R. J.; Shaw, D. W.; Rosenbaum, E. *AAPG Bull.*, in press.

(22) Brodkey, R. S.; Hershey, H. C. *Transport Phenomena: A Unified Approach*; McGraw Hill, Inc.: New York, 1988.

(23) NIST. *NIST Chemistry Webbook*; NIST: Washington, DC, 2007.

(24) U.S. Coast Guard. Selected properties of fresh water, sea water, ice, and air. In *Chemical Hazards Response Information System*; p 4. http://www.chrismanual.com/intro.pdf, 181 pp (accessed 9/24/2007).

(25) Gustafsson, S. E.; Karawacki, E.; Chohan, M. A. *J. Phys. D: Appl. Phys.* **1986**, *19*, 727.

(26) Berendsen, H. J. C.; Grigera, J. R.; Straatsma, T. P. *J. Phys. Chem.* **1987**, *91*, 6269.

(27) Horn, H. W.; Swope, W. C.; Pitera, J. W.; Madura, J. D.; Dick, T. J.; Hura, G. L.; Head-Gordon, T. *J. Chem. Phys.* **2004**, *120*, 9665.

(28) Rick, S. W.; Stuart, S. J.; Berne, B. J. *J. Chem. Phys.* **1994**, *101*, 6141.

(29) Tse, J. S.; Klein, M. L.; McDonald, I. R. *J. Chem. Phys.* **1984**, *81*, 6146.

(30) English, N. J.; MacElroy, J. M. D. *J. Comput. Chem.* **2003**, *24*, 1569.

(31) English, N. J.; Johnson, J. K.; Taylor, C. E. *J. Chem. Phys.* **2005**, *123*, 244503.

(32) English, N. J.; MacElroy, J. M. D. *J. Chem. Phys.* **2004**, *120*, 10247.

(33) Dang, L. X. *J. Chem. Phys.* **1992**, *97*, 2659.

(34) Brodholt, J.; Sampoli, M.; Vallauri, R. *Mol. Phys.* **1995**, *86*, 149.

(35) Dang, L. X.; Chang, T.-M. *J. Chem. Phys.* **1997**, *106*, 8149.

(36) Burnham, C. J.; Li, J.; Xantheas, S. S.; Leslie, M. *J. Chem. Phys.***1999**, *110*, 4566.

(37) Cho, K.-H.; No, K. T.; Scheraga, H. A. *J. Mol. Struct.* **2002**, *641*, 77.

(38) Ren, P.; Ponder, J. W. *J. Phys. Chem. B* **2003**, *107*, 5933.

(39) Lamoureux, G.; MacKerell, J. A. D.; Roux, B. *J. Chem. Phys.* **2003**, *119*, 5185.

(40) Wu, Y.; Yang, Z. Z. *J. Phys. Chem. A* **2004**, *108*, 7563.

(41) Yu, H.; van Gunsteren, W. F. *J. Chem. Phys.* **2004**, *121*, 9549.

(42) Berendsen, H. J. C.; Postma, J. P. M.; Van Gunsteren, W. F.; Hermans, J. Interaction models for water in relation to protein hydration, in *Intermolecular Forces*; Pullman, B., Ed.; Reidel: Dordrecht, The Netherlands, 1981; p 331−342.

(43) Jorgensen, W. L.; Chandrasekhar, J.; Madura, J. D.; Impey, R. W.; Klein, M. L. *J. Chem. Phys.* **1983**, *79*, 926.

(44) Lekner, J. *Physica A (Amsterdam)* **1989**, *157*, 826.

(45) Lekner, J. *Physica A (Amsterdam)* **1991**, *176*, 485.

(46) English, N. J.; MacElroy, J. M. D. *Mol. Phys.* **2002**, *100*, 3753.

(47) Allen, M. P.; Tildesley, D. J. *Computer Simulation of Liquids*; Clarendon: Oxford, 1987.

(48) Martyna, G.; Tuckerman, M.; Tobias, D.; Klein, M. *Mol. Phys.* **1996**, *87*, 1117.

(49) Andersen, H. C. *J. Comput. Phys.* **1983**, *52*, 24.

(50) McMullan, R. K.; Jeffrey, G. A. *J. Chem. Phys.* **1965**, *42*, 2725.

(51) Bernal, J. D.; Fowler, R. H. *J. Chem. Phys.* **1933**, *1*, 515.

(52) Rahman, A.; Stillinger, F. H. *J. Chem. Phys.* **1972**, *57*, 4009.

(53) Hayward, J. A.; Reimers, J. R. *J. Chem. Phys.* **1997**, *106*, 1518.

(54) Eisenberg, D.; Kauzmann, W. *The Structure and Properties of Water*; Oxford University Press: Oxford, 1969.

(55) Baez, L. A.; Clancy, P. *Ann. N.Y. Acad. Sci.* **1994**, *715*, 177.

(56) Izaguirre, J. A.; Reich, S.; Skeel, R. D. *J. Chem. Phys.* **1999**, *110*, 9853.

(57) Vogelsang, R.; Hoheisel, C. *Phys. Rev. A (Amsterdam)* **1987**, *35*, 3487.

(58) IAPWS. *Revised Release on the IAPS Formulation 1985 for the Thermal Conductivity of Ordinary Water Substances*; 1998; p 23. http://www.iapws.org/ (accessed 9/24/07).

(59) Stern, L. A.; Kirby, S. H.; Durham, W. B. *Science* **1996**, *273*, 1843.

(60) Stern, L. A.; Kirby, S. H.; Durham, W. B. *Energy Fuels* **1998**, *12*, 201.

(61) Waite, W. F., personal communication.

(62) Zhong, Y.; Rogers, R. E. *Chem. Eng. Sci.* **2000**, *55*, 4175.

(63) Nicholson, B. F.; Clancy, P.; Rick, S. W. *J. Cryst. Growth* **2006**, *293*, 78.

(64) Vega, C.; Sanz, E.; Abascal, J. L. F. *J. Chem. Phys.* **2005**, *122*, 114507.

(65) Rick, S. W. *J. Chem. Phys.* **2001**, *114*, 2276.

(66) Parrinello, M.; Rahman, A. *Phys. Rev. Lett.* **1980**, *45*, 1196.

(67) English, N. J. *Mol. Phys.* **2005**, *103*, 1945.

(68) U.S. Army Corps of Engineers, *Review of ice processes and properties*, Chapter 2 in *Engineering and Design: Ice Engineering*, 2002; Manual No. EM 1110-2-1612; p. 2-3, available at http://www.usace.army.mil/publications/eng-manuals/em1110-2-1612/toc.htm (accessed 9/25/07).

(69) Lunardini, V. J. *Heat Transfer in Cold Climates*; Van Nostrand Reinhold: New York, 1981.

(70) Ohara, T. *J. Chem. Phys.* **1999**, *111*, 6492.

(71) Press, W. H.; Flannery, B. P.; Teukolsky, S. A.; Vetterling, W. T. *Numerical Recipes*, 2nd ed.; Cambridge University Press: Cambridge, 1992.